Image Processing and CFD Simulation Method Comparison in Determining and Visualizing Fluid Flow of a Marine UAV

Sinung Widiyanto[1*], G. A. P. Poundra[2], Tri Agung Kristiyono[2], Widyawasta[3], Sayuti Syamsuar[3]

***Abstract*— An investigation of marine UAV performance with various designs have done successfully. The analysis was based on resistance criteria identification both aerodynamically and hydrodynamic. The calculations were conducted with the assistance of image processing as the experimental attempt and High-Fidelity Computational Fluid Dynamics (CFD) software code to simulate the fluid flow on the fuselage designs, pontoons, and image processing. Both methods compared to acquire the silver line in which way they can collaborate to create new way of testing. Furthermore, mathematical calculations and Image processing works refereeing were also performed as the attempt for validations and conclusion.**

***Keywords*—Computational fluid dynamics, Fluid flow, Image processing, Marine UAV**

I. INTRODUCTION

The usage of image processing in topological identification helps enhancing the quality of object or phenomenon observation. The impact of image-processing becomes more evident when the hydrodynamic and aerodynamic behavior, i.e. X-, Y-, Z- velocity and static pressure of an object interacted with fluids are explored [1]. The implementation of the two methods may help indicates particle segregation, such as in the presence of small bubbles and turbulence, while particle mixing improves at a velocity above the minimum fluidization velocity [2].

Since turbulence due to a fluid-object interactions are usually random, based on the geometry of the object and yet so influential to the phenomenon arise, a clear picture of it need to be acquired to identify the source, pattern, and the form to find solutions for controlling the turbulence based on the requirement. Thus, a combination of image processing and high fidelity CFD are needed. After the image acquisition, image denoising, thresholding, logical and mask operations are applied correspondingly for the boundary discrimination, based on which an algorithm has been developed to determine the object and the phenomenon [3].

In the past several years, Computational Fluid Dynamics (CFD) methods with different levels of complexity were developed for aerodynamics and hydrodynamics investigations and have been extensively used to solve fluid dynamics problems [4] One variable which can be calculated using the CFD method by analyzing the fluid – object interactions and all the forces acting during the phenomenon is resistance. In the framework of CFD codes, the numerical prediction is made by using unsteady Reynolds-Averaged Navier-Stokes (URANS) computations coupled with the equations of rigid body motion [5].

II. METHOD

A. CFD (Computational Fluid Dynamics)

The CFD software which being utilized in this research is the Eulerian - mesh based methods CFD with user interface. Multiphase and moving parts modelling were offered by the software especially on lubrication workflows such as gearboxes and electric motor drives [6]. Compared to the smoothed-particle hydrodynamics (SPH) CFD code which using Lagrangian method, the Eulerian-based CFD is a simpler software to utilize [7].

The software features the highest fidelity Wall-Modeled Large Eddy Simulation (WMLES) for the turbulence modelling approach for the simulation [6]. The decision to choose this turbulence model was due to its effectiveness to improve the computational efficiency of two-phase flow. The high Reynolds number of the actual flow and the complexity of multi-scale interaction between the turbulence and particles pose a great challenge to the numerical simulation [8]. The accuracy of WMLES model depends on both the sub grid-scale (SGS) model which refers to the representation of important small – scale physical process that occur at length-scales that cannot be adequately resolved on a computational mesh and wall model [8].

The simulation was conditioned in incompressible flow. Hence, the boundary layer was made in a large size to prevent the blockage effect and to neglect the near wall treatment. The underlying state-of-the-art large eddy simulation (LES), based on the Wall-Adapting Local Eddy (WALE) viscosity model, provides a consistent local eddy-viscosity and near wall behavior [6]. Thus, an efficient way to do the simulation is needed. A hybrid strategy in combining Reynolds-averaged Navier-Stokes (RANS) and large eddy simulation (LES) methods was done to simulate turbulent flows of practical relevance [9].

[1] Department Magister of Ocean Engineering, Universitas Hang Tuah Surabaya, Jalan Arief Rachman Hakim No. 150 Sukolilo, Surabaya, Postal Code 61111, Indonesia. E-mail: sinung.widiyanto@hangtuah.ac.id

[2] Department of Naval Architects, Universitas Hang Tuah Surabaya, Jalan Arief Rachman Hakim No. 150 Sukolilo, Surabaya, Postal Code 61111, Indonesia. E-mail: prabhawatya.poundra@hangtuah.ac.id

[3] BRIN, Rumah Program Penerbangan dan Antariksa, Indonesia. E-mail: widyawast@brin.go.id, sayuti.samsuar@brin.go.id

B. Design and 3D Modelling

3D modelling must be done to translate the blueprint into virtual objects which can be read by the software. The process in this stage consists of part modelling (fuselage, landing gears and tail) and assembly. Throughout the activity, details may be checked while revising the blueprint in advance to create an optimized design.

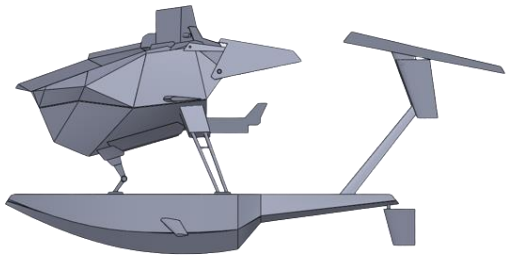

Figure 1. 2D Model Side View

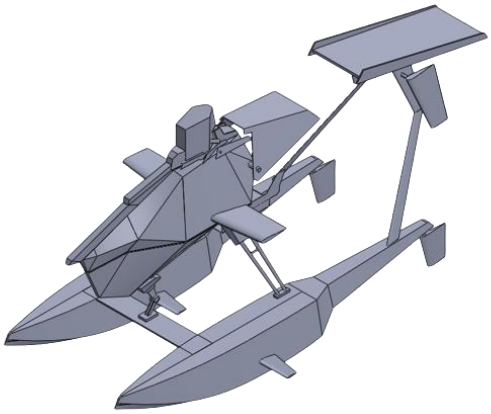

Figure 2. 3D Model Sample

This attempt was very important since the CFD simulation software only be able to receive and process 3D models which set to be solid (not surface). The solid object prevents unrequired fluid particle leakages along the body of the specimen that shall assist the preservation of the calculation accuracy. These leaks can be an obstacle in the research due to other problem may be raised in the process. Leaks or imperfect specimen may generate eddies or turbulence which affecting the performance of the vehicle (both in speed and power prediction and maneuverability simulation).

C. CFD Simulation

During the calculation using CFD, the environment was set with multiphase flow model. The setting was chosen to replicate a water channel due to the ability of the UAV to work on both air and water. Since the performance of the vehicle tested in both CFD simulation and image processing, particle-based tracking was chosen as the method to run the calculation. Particle-based tracking was useful for comprehensive fluid dynamic calculation at particle level with accurate modelling and intra-particle gradients description for particle movement [10] The boundary layer was set at the dimension of 200 m length, 45 m width, and 45 m height.

For the water channel set in calm water with no external wind speed interaction. Hence, the Beaufort wind scale and the inlet wave function equals to $y < 0\ m$. The fluid surface set to $y < 1.15\ m$ based on the design draft of the vehicle. Besides that, the boundary layer includes no channel walls velocity lawX, -9.81 $m.s^{-2}$ external acceleration laws in respect of Y axis, and isothermal thermal model. Fluid materials are divided into two (gas and liquid) for multiphase simulation with normal operating temperature around 288.15 K.

For turbulence modelling, the research using Wall-Modelled Large Eddy Simulation (WMLES) to trace the high Reynolds number in complex configurations both in compressible and incompressible flow. This type of turbulence model provides accurate wall flows while avoiding direct control of near-wall resolution. Secondly, it also treating arbitrarily complex geometries in Cartesian grids efficiently [11], [12]. Numerical scheme for WMLES must be non-dissipative and provide sufficient dissipation to handle flow discontinuities, where:

$$\hat{f}_{i+1/2} = (1-\alpha)\hat{f}^{Cent}_{i+1/2} + \alpha\hat{f}^{Diss}_{i+1/2} \quad (1)$$

For the interior, *Cent* consists of fourth-order, centered, kinetic energy and an entropy preserving (KEEP) scheme where can be written as:

$$KE_t = \int^{\Omega} K_t\, dV \quad (2)$$

$$K_t = \frac{1}{2}u_i u_i \quad (3)$$

And the *Diss* consists the third weighted essentially non-oscillatory (WENO) scheme with the conservative finite difference operator as follows,

$$\frac{\partial f}{\partial x} = \frac{1}{\Delta x}\left(h_{i+\frac{1}{2}} - h_{i-\frac{1}{2}}\right) = \frac{1}{\Delta x}\left(\hat{f}_{i+\frac{1}{2}} - \hat{f}_{i-\frac{1}{2}}\right) + \varphi(\Delta x^{2n-1}) \quad (4)$$

The governing equations for LES are obtained by spatial filtering of the incompressible Navier-Stokes equations, where [13]:

$$\frac{\partial}{\partial t}(\bar{u}_i) + \frac{\partial}{\partial x_j}(\bar{u}_i\bar{u}_j) - v\frac{\partial^2\bar{u}_i}{\partial x_j \partial x_j} = -\frac{\partial \bar{p}}{\partial x_i} - \frac{\partial \tau_{ij}}{\partial x_j} \quad (5)$$

The simulation was conducted on a budget gaming computer with specifications which can be mentioned as follows,

Processor : AMD Ryzen 7 3750H with Radeon Vega Mobile Gfx (8 CPUs) ~ 2.3 GHz
RAM : 16384 MB
BIOS : FX505DT .316
GPU 1 : AMD Radeon™ RX Vega 10 Graphics
GPU 2 : NVIDIA GeForce GTX 1650
DirectX Version : DirectX 12

The process was mainly conducted using the processor, while the GPU was still being used but without the ray tracing technology.

D. Image Processing Classification

The image processing method in this experiment is using color classification. The purpose of the Color Classification method is to determine the max flow and pressure created by the UAV Model. The UAV model in CFD, are the base line to calculate the max flow and pressure. The result from CFD simulation will contain

video with difference colors information, such as size, pressure colors, and shape of the wave. Using Color classification, the data in real model can compare with the calculation from CFD simulation.

Color classification comparing the differences of color using this step of technique:

1. Image Filtering.
   The pixel value of an image can be modified for the purpose of getting the difference information. Reducing the unwilling color will create segregation or boundaries.
2. Feature Extraction.
   The area pixel segment creates some pattern. Recognizing pattern color or the shape are the method of the feature extraction. The detected feature will be added to create an image database.
3. Color Classification.
   The image database generated by the Pixel Color information can be used to determine differences and classify object. The classified color object is used as data base in the next process.
4. Image Recognition.
   The database of image is the base line to recognize new information from new image.
5. Pixel Counting.
   Each image pixel that is already recognized using the image recognition process, has a lot of information. counting the pixel is process to is to determine the calculate the information due to the same color pattern.

III. Results and Discussion

The simulation using high fidelity CFD for this research have done successfully. The method perfectly visualized the turbulence flow generated around the body of the vehicle structured based on the amount of fluid-object interactions. The flow pattern however, only can be seen clearly using the stream arrows and hardly seen using stream marker due to the lack of ray tracing ability of the hardware GPU. Hence, low specification computer may not be able to run the program properly. However to run the image processing is much easer than the CFD Simulation. The result of the image processing classification determine the new technique to approach the new solution of the UAVs testing. Object recognition from the image processing can be determined from the collection of database of CFD simulation process. The water spray, fluid movement, and UAVs Object characteristic calculate in pixel counting, saved as data base.

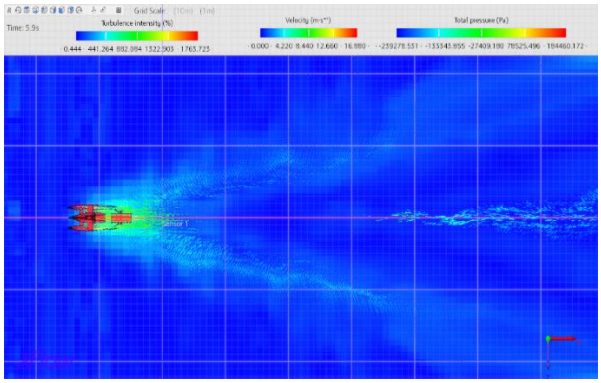

Figure 3. CFD Result (Taxiing Condition) Top View

Although the fluid flow pattern is blurred due to the hardware ability as shown in Figure 4, the results, such as: turbulence intensity, velocity, total pressure, etc. still may be counted with the method intensively. The large eddy simulation (LES) and high fidelity allows a detailed and sophisticated geometric model to be simulated with nearly zero coarse generated surface. This part is very important because the ability of the software to capture and process every inch of the geometry results in a better flow pattern.

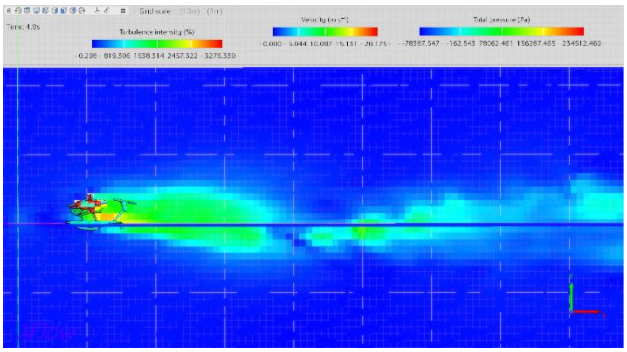

Figure 4. CFD Result (Taxiing Condition) Side View

The other thing that a high fidelity CFD less able to visualize is the distribution of fluid flow variable along the body of the object. In general, the user can see the difference of the distributions in different locations and it is still quite understandable. However, user may not be able to pin point exactly in detail as represented in Figure 4 without ray tracing GPU. On the other hand, the process of solving the fluid dynamic problems using high fidelity CFD is less time consuming as it involves less mesh (although not completely neglecting it like smoothed-particle hydrodynamics (SPH) method).

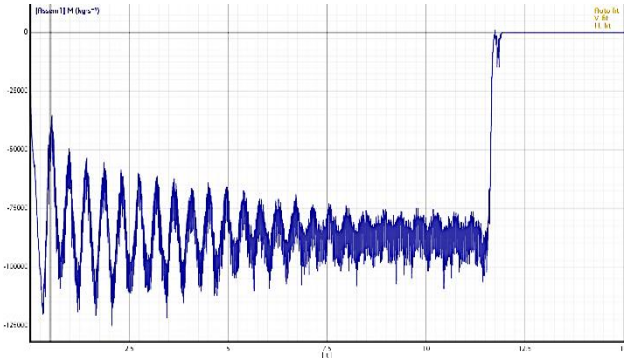

Figure 5. Mass Flow (Taxiing Condition)

The calculation graphs of the high fidelity CFD consists of truncation error based on the scheme being utilized which related to the numerical flux derivative at x_i and satisfied the equation as follows,

$$\left.\frac{\partial f}{\partial x}\right|_{x=x_i} = \frac{h_{i+1/2}-h_{i+1/2}}{\Delta x} \approx \frac{\bar{f}_{i+1/2}-\bar{f}_{i-1/2}}{\Delta x} \qquad (6)$$

Where the truncation error obtaining flux at $x_{i+1/2}$ can be written as

$$\hat{f}_{i+1/2} = h_{i+1/2} - A\left.\frac{\partial^3 f}{\partial x^3}\right|_{x=x_i} \Delta x^3 \qquad (7)$$

The truncation error in each result vary due to the phenomenon and variables measures. The mass flow shown in Figure 5 have more truncation error compared to the total pressure represented in Figure 6. Due to no reverse flow during the simulation, the vehicle received no mass flow from the oscillatory effect due to the wall

deflection which reduces the truncation error throughout the time steps as shown in Figure 5. In contrast with the total pressure, the mass flow acquired various range of truncation error due to the base variable difference which being the focus of the calculation. While the mass flow focuses on the force which delivered to the fluids, the total pressure focus on the force which delivered to the vehicle which make more truncation errors occur in the lower amount time step compared to the higher amount in mass flow.

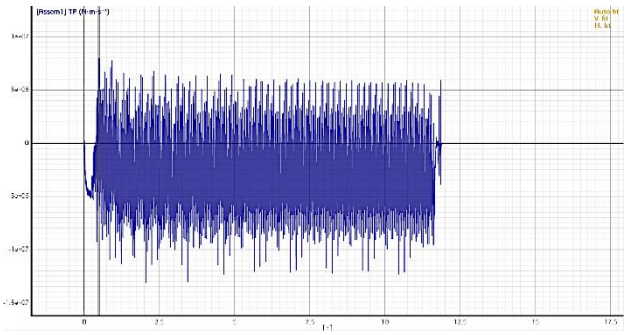

Figure 6. Total Pressure (Taxiing Condition)

The calculation of the overall kinetic energy is represented in Figure 7. The result shows that the increase of the energy grown rapidly throughout the time steps. Compared to the total pressure, mass flow, and stability parameter, this variable fluctuates smoother. This is due to the particle velocity which increase as the dynamic of the fluids grown faster over time. From the result in Figure 7, building condition in each time step also provided implicitly along with its fluctuation which satisfy viscous three-dimensional periodic solutions,

$$u_x = \frac{4\sqrt{2}}{3\sqrt{3}} U_0[sin\,(kx - \pi/3)\,cos(ky + \pi/3)sin(kz + \pi/2) - cos(kz - \pi/3)sin(kx + \pi/2)sin(ky + \pi/2)]\,e^{-3\nu k^2 t} \quad (8)$$

$$u_y = \frac{4\sqrt{2}}{3\sqrt{3}} U_0[sin\,(ky - \pi/3)\,cos(kz + \pi/3)sin(kx + \pi/2) - cos(kx - \pi/3)sin(ky + \pi/2)sin(kz + \pi/2)]\,e^{-3\nu k^2 t} \quad (9)$$

$$u_z = \frac{4\sqrt{2}}{3\sqrt{3}} U_0[sin\,(kz - \pi/3)\,cos(kx + \pi/3)sin(ky + \pi/2) - cos(ky - \pi/3)sin(kz + \pi/2)sin(kx + \pi/2)]\,e^{-3\nu k^2 t} \quad (10)$$

While also satisfy the continuity equation in incompressible condition. During in this condition, ρ does not change for any fluid particle and its material derivative vanishes. Hence,

$$\partial_x u_x + \partial_y u_y + \partial_z u_z = 0 \quad (11)$$

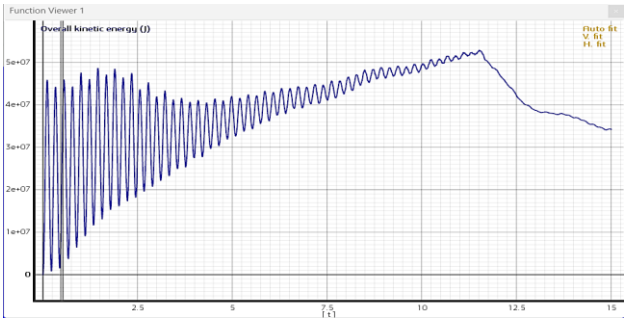

Figure 7. Overall Kinetic Energy (Taxiing Condition)

In terms of computational stability, High Fidelity CFD provides a quite satisfying result as shown in Figure 8. For a simulation that runs on budget computer specification it is difficult to trace the equilibrium path throughout the process due to complexity of the simulation. This computational instability surely may affect the amount of truncation errors occurrences in other variable computation.

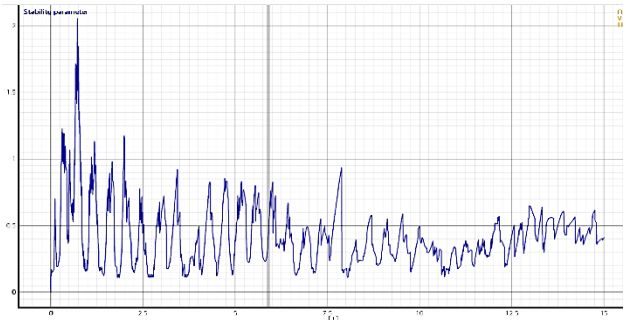

Figure 8. Stability Parameter (Taxiing Condition)

IV. CONCLUSION

According to the results of the research, several conclusions can be drawn from the comparative methods in simulating fluid dynamics digitally. The factors which effects the performance and the result of the simulation can be varied, from hardware compatibility to model sample which resulting accuracy difference. Those conclusions can be mentioned as follows,

1. High fidelity CFD, although can process the geometric object in detail with very small coarse parts, still need a computer with ray tracing technology to visualize the fluid flow pattern.
2. Although lacking in visual result, high fidelity CFD still have the ability to provide a fine fluid dynamic numerical calculation.
3. The image Processing Classification only determines the counting result of the CFD. For the future research comparing actual data with real model will be next topic.

REFERENCES

[1] S. Kyrimis, R. Raja, and L.-M. Armstrong, "Image processing of computed tomography scanned poly-dispersed beds for computational fluid dynamic studies," *Advanced Powder Technology*, vol. 34, no. 11, p. 104199, 2023.

[2] R. Aramesh, V. Akbari, A. Shamiri, M. A. Hussain, and N. Aghamohammadi, "Hydrodynamics and particle mixing/segregation measurements in an industrial gas phase olefin polymerization reactor using image processing technique and CFD-PBM model," *Measurement*, vol. 83, pp. 106–122, 2016.

[3] J. Yang, R. W. Breault, and S. L. Rowan, "Applying image processing methods to study hydrodynamic characteristics in a rectangular spouted bed," *Chem Eng Sci*, vol. 188, pp. 238–251, 2018.

[4] M. Ye, H.-C. Chen, and A. Koop, "High-fidelity CFD simulations for the wake characteristics of the NTNU BT1 wind turbine," *Energy*, vol. 265, p. 126285, 2023.

[5] D. Kim, T. Tezdogan, and A. Incecik, "A high-fidelity CFD-based model for the prediction of ship manoeuvrability in currents," *Ocean Engineering*, vol. 256, p. 111492, 2022.

[6] J. Wu, X. Wang, X. Pei, and T. Hou, "Design and simulation analysis of mantle cavity of jet thruster," in *2023 International Conference on Frontiers of Robotics and Software Engineering (FRSE)*, IEEE, pp. 347–354, 2023.

[7] F. Zhang *et al.*, "DualSPHysics: a numerical tool to simulate real breakwaters," *Journal of Hydrodynamics*, vol. 30, pp. 95–105, 2018.

[8] T. Jin, Z. Chen, and P. Wang, "Performance assessment of wall-modeled large-eddy simulation for modeling aeolian two-phase flow," *European Journal of Mechanics-B/Fluids*, vol. 100, pp. 291–301, 2023.

[9] M. D. Mays, S. Lardeau, and S. Laizet, "Capturing the drag crisis in the flow around a smooth cylinder using a hybrid RANS-LES model on coarse meshes," *Int J Heat Fluid Flow*, vol. 103, p. 109203, 2023.

[10] L. von Berg, A. Anca-Couce, C. Hochenauer, and R. Scharler, "Multi-scale modelling of a fluidized bed biomass gasifier of industrial size (1 MW) using a detailed particle model coupled to CFD: Proof of feasibility and advantages over simplified approaches," *Energy Convers Manag*, vol. 286, p. 117070, 2023.

[11] S. Iousef, H. Montazeri, B. Blocken, and P. J. V van Wesemael, "Wall-resolved versus wall-modeled LES of the flow field and surface forced convective heat transfer for a low-rise building," *Build Environ*, vol. 244, p. 110678, 2023.

[12] F. De Vanna, G. Baldan, F. Picano, and E. Benini, "On the coupling between wall-modeled LES and immersed boundary method towards applicative compressible flow simulations," *Comput Fluids*, vol. 266, p. 106058, 2023.

[13] X. Ren, H. Su, H.-H. Yu, and Z. Yan, "Wall-modeled large eddy simulation and detached eddy simulation of wall-mounted separated flow via OpenFOAM," *Aerospace*, vol. 9, no. 12, p. 759, 2022.